On-chip photothermal gas sensor based on a lithium niobate rib waveguide

Yue Yan [a,1], Hanke Feng [b,1], Cheng Wang [b,*], Wei Ren [a,*]

[a] *Department of Mechanical and Automation Engineering, The Chinese University of Hong Kong, New Territories, Hong Kong SAR, China*
[b] *Department of Electrical Engineering & State Key Laboratory of Terahertz and Millimeter Waves, City University of Hong Kong, Kowloon, Hong Kong SAR, China*

A B S T R A C T

On-chip optical gas sensors have attracted a lot of attention in many fields such as the internet of things and point-of-care diagnosis due to their compactness and high scalability. However, the current laser-based on-chip absorption gas sensors have limited performance caused by weak gas absorbance and strong interference fringe noise. Here, we report sensitive on-chip photothermal gas detection on an integrated lithium niobate photonic platform. The evanescent wave of the frequency-modulated pump light (2004 nm) on a nanophotonic lithium niobate rib waveguide (length of 91.2 mm) is absorbed by the target gas molecules (carbon dioxide, CO_2), leading to the significant refractive index modulation of the rib waveguide due to the photothermal effect. A probe light (1550 nm) transmitted through the same waveguide undergoes the photothermal-induced phase modulation, which is sensitively detected by a heterodyne interferometer. As a proof of concept, we demonstrate the on-chip photothermal detection of CO_2 with a minimum detection limit of 870 ppm. This work provides new insight for future on-chip gas sensor development with high sensitivity and robustness.

1. Introduction

On-chip gas sensing has attracted significant attention due to its small size, low cost, and prospects for high-density integration, with potential applications ranging from environmental monitoring to biomedical diagnosis [1,2]. By integrating the internet of things (IoT) technology, on-chip gas sensors are promising for building large sensing networks for distributed monitoring applications. In biomedical diagnosis, compact on-chip gas sensors are important for point-of-care diagnostic tools like portable breath analyzers [3]. Moreover, with the increasingly mature technologies of integrated photonics and foundry services, it is possible to develop highly scalable on-chip sensing systems densely integrated with gas sensors and a full range of functional photonic elements such as interferometers and modulators [4–6].

One common method for developing an on-chip gas sensor is to utilize the interaction between the evanescent field and the analyte [7, 8]. Evanescent-wave on-chip gas sensors have demonstrated a detection limit down to 100 parts-per-million (ppm) on a silicon waveguide [9]. Migrating the laser absorption sensor to an integrated photonic platform enables a monolithic sensing chip with substantial cost-benefit and scalability [10,11]. The prevalent challenge faced by conventional on-chip waveguide gas sensors involves the significant degradation in

sensor performance caused by etalon fringe noise. Several attempts have been made to mitigate this issue through the implementation of various algorithms [12–14], but their performances are limited and without generality. Mid-infrared on-chip waveguide gas sensors with detection limit of several ppm level were also demonstrated by leveraging the extraordinary evanescent field confinement factor beyond free-space [7, 8]. These waveguide designs demonstrated minimized facet reflections, contributing to the mitigation of fringes noise. Nonetheless, the sensitivity can be restricted due to the waveguide's limited length and relatively substantial propagation loss.

Instead of directly measuring light intensity attenuation, photothermal spectroscopy (PTS) is an emerging method with high sensitivity by probing the photothermal-induced phase change via interferometry [15–17]. Recently, by taking advantage of the stronger optical field confinement to enhance the photothermal effect, PTS in a hollow-core fiber (HCF) enables sensitive gas detection with extremely high sensitivity and dynamic range [18–20]. In a typical PTS system with a pump-probe configuration, gas absorption of the modulated pump light dissipates heat to the surrounding which subsequently modulates the refractive index (RI) of the gas medium. The RI variation modulates the phase of a following probe laser that propagates through the same path as the pump laser in the gas medium. Only the photothermal-induced

---

phase modulation signal can be picked up by the heterodyne interferometer, which effectively eliminates the background interference fringe noise. Additionally, compared to HCFs with a core diameter of tens of micrometers, realizing PTS in a sub-micrometer integrated photonic waveguide typically further enhances the photothermal effect. Hence, it usually increases the detection signal-to-noise ratio (SNR) by performing PTS in a photonic device such as the nanophotonic lithium niobate waveguide.

Nanophotonic lithium niobate (LiNbO$_3$, LN) is a promising platform for high-sensitivity on-chip PTS considering its wide transparent window (350 nm – 5 μm), low optical loss, high thermo-optic coefficient and good scalability [21,22]. More importantly, it is endowed with a variety of functional nanophotonic devices such as high-quality-factor micro-resonators, high-bandwidth and low-power optical modulators, broadband frequency-comb sources, and on-chip spectrometers [23–27]. The prospect of integrating multi-functional chip-scale devices on a single nanophotonic LN-on-insulator chip potentially enables a compact sensing platform for smart, low cost and highly scalable sensing applications.

Here, we report photothermal gas sensing on a nanophotonic LN platform for the first time. Using a 91.2 mm low-loss rib waveguide fabricated on an LN thin film, we demonstrate the detection of carbon dioxide (CO$_2$) at 4989.97 cm^{-1} (2004 nm) as a proof of concept. This on-chip photothermal gas sensor achieves a detection limit of 870 ppm with 190 s integration time, which is much more sensitive and robust compared to the direct absorption spectroscopy conducted on the same waveguide.

2. Method

2.1. Waveguide fabrication

The LN waveguide dimensions are chosen to support single transverse electric (TE) mode propagation and provide substantial evanescent field ratio in the air-cladding, as shown in the inset figure in Fig. 1 (c), where $h_1 = h_2 = 250$ nm and $w = 800$ nm. And the LN waveguide is fabricated from a commercially available LN thin film (NANOLN) with a thickness of 500 nm. Designed patterns are first defined in hydrogen silsesquioxane (HSQ) using electron-beam lithography (EBL, 50 keV) and then transferred into the LN layer using optimized argon plasma-based reactive ion etching (RIE). The LN etch depth is 250 nm, leaving a 250-nm-thick slab. Fig. 1(a) shows the fabricated meandering LN waveguide with a total physical length of 91.2 mm; the SEM images of the cross section and the side view of the LN waveguide are illustrated in Fig. 1(b) and 1(c). The waveguide sidewall has a 60° trapezoidal shape according to the actual LN nanofabrication process. The electric field of the TE$_0$ mode at 2004 nm is analyzed by the finite element method, the RI of the waveguide materials (LN and SiO$_2$) at wavelength $\lambda = 2$ μm can be found in literatures [28,29]. The effective RI (n_{eff}) of the TE$_0$ mode is calculated to be 1.75. A portion of the evanescent field exists in the air-cladding for gas absorption. The evanescent field factor can be determined by [30]:
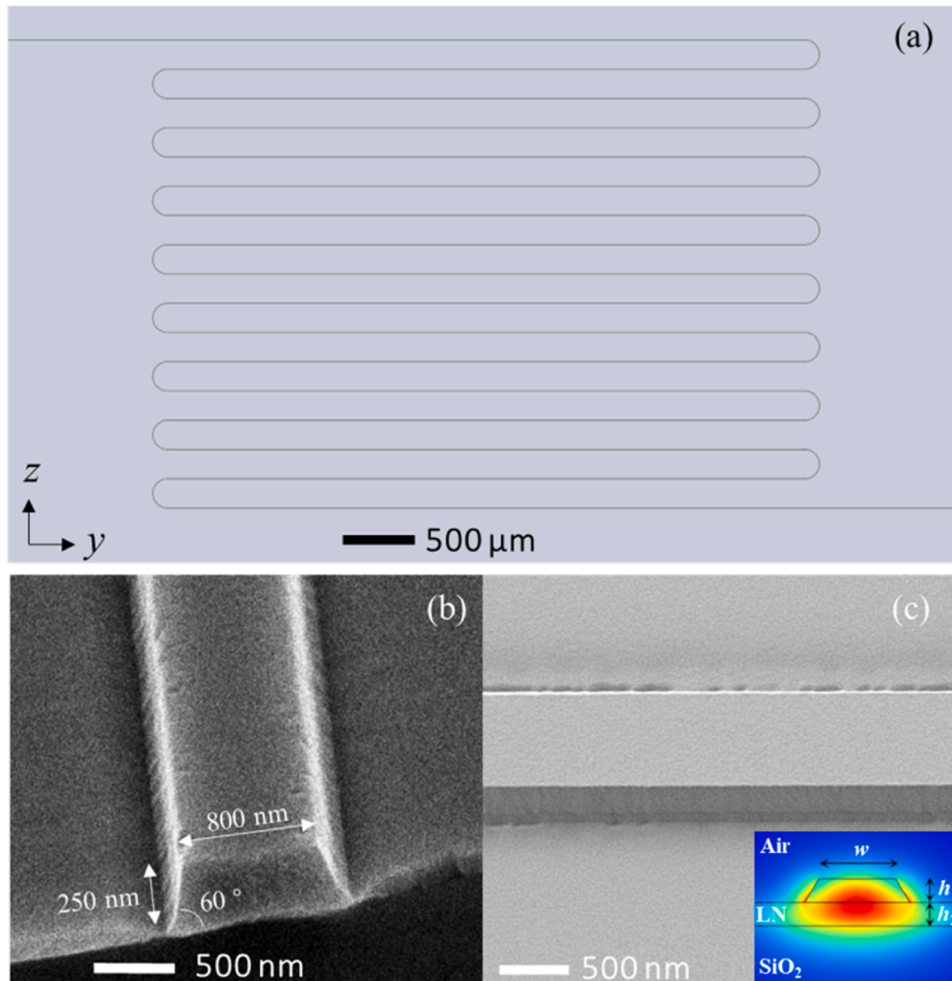
Fig. 1. (a) False-color wide-field microscope image of the LN waveguide, the bending region has a radius of $r = 100$ μm. (b) SEM image of the cross section. (c) SEM image from the side-view. Inset: LN waveguide model and electric field profile of the TE$_0$ mode at 2004 nm.

$$\Gamma_{air} = n_g \bullet \frac{\iint_{Air} \varepsilon(x,z) \bullet |E|^2 dxdz}{\iint_{-\infty}^{+\infty} \varepsilon(x,z) \bullet |E|^2 dxdz}. \tag{1}$$

where Γ_{air} is the evanescent field factor in the air-cladding, ε is the permittivity of each layer of the LN waveguide, E is the electric field, and n_g is the group index of the TE$_0$ mode. As a result, the evanescent field factor in the air-cladding is calculated to be 7.4% at the pump wavelength of 2004 nm.

2.2. Coupling and propagation loss

To evaluate the coupling and propagation loss, we characterize a LN ring resonator at wavelength around 2004 nm. The ring resonator has a radius of $r = 100$ µm and has the same waveguide structure as the sensing waveguide. The cavity mode is presented in Fig. 2. The analysis reveals a full width at half maximum (FWHM) $\Delta\lambda = 0.011$ nm with free spectral range (FSR) of 2.9 nm. Thus, the finesse of the cavity is deduced as $F = 264$, corresponding to a round trip loss of 0.11 dB. It is important to emphasize that this calculated loss includes both the propagation loss and the bending loss. The pure bending round trip loss is calculated to be 0.038 dB from theoretical analysis with the finite-difference time-domain (FDTD) method, more details can be found in the Supplementary Note 1. Consequently, the propagation loss is now estimated to be 0.072 dB, equivalent to 1.2 dB/cm. Measuring the transmitted laser power through the 91.2 mm waveguide to be 50 µW for an 8 mW pump laser input yields a total loss of 22 dB. Hence, the total coupling loss is deduced as 11 dB, resulting in a coupling loss of 5.5 dB/facet.

2.3. Fundamentals of on-chip photothermal spectroscopy

Gas absorption of the pump laser in the air-cladding dissipates the localized heat to the solid waveguide, which causes the temperature variation of the waveguide. Fig. 3 depicts the basic physical processes involved in the proposed on-chip photothermal gas sensing. Unlike the conventional photothermal detection in an HCF or free space, on-chip photothermal detection mainly utilizes the RI change in a solid waveguide instead of gas. The photothermal-induced RI change causes the phase shift of the probe laser propagating in the waveguide. Since the thermo-optic coefficient of air (-0.91×10^{-6}/K [31]) is much smaller than that of LN (extraordinary direction: 32.4×10^{-6}/K [32]), the on-chip phase modulation can be substantially enhanced compared to that achieved in the gas medium.

Fig. 4(a) depicts the simulated heat source distribution originated from CO_2 absorption with an absorption coefficient of 0.12 cm^{-1} at the pump wavelength of 2004 nm and optical power of 1 mW. The on-chip photothermal dynamics and the simulation details are provided in Supplementary Note 2. The peak heat density reaches as high as 8.7×10^9 W/m^3 due to the strong optical confinement of the guided TE$_0$
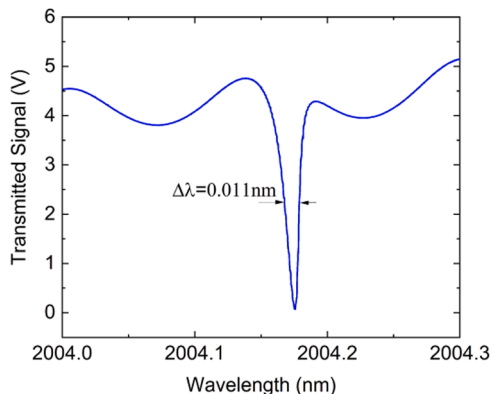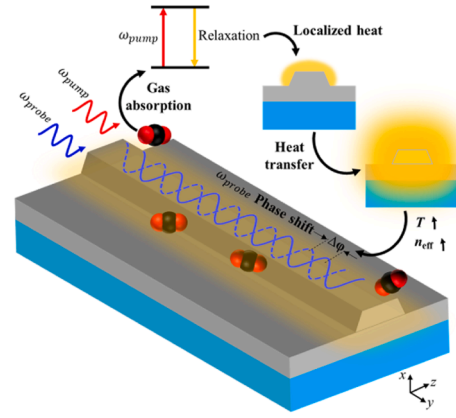

Fig. 3. Principle of on-chip photothermal gas sensing.

mode. The heat source is sinusoidally modulated at the modulation frequency of the pump laser. At the center of the LN waveguide, Fig. 4(b) shows the time-dependent photothermal modulation dynamics with the pump laser frequency modulated at 5 kHz. The temperature of the LN waveguide increases from the initial 295 K because of the heat conduction from the air-cladding to the waveguide. The temperature variation ΔT reaches a plateau level after 100 ms, indicating the steady state of heat conduction. Besides the overall trend of temperature increase, a periodic variation of temperature with a small amplitude of 0.83 mK is observed as shown in the inset graph of Fig. 4(b). This periodic temperature variation induces an RI modulation to be detected by the probe laser beam. Due to the birefringence of the LN crystal [32], it has the largest positive thermo-optical coefficient along the z-direction, which aligns with the major electric field component of the TE$_0$ mode in this study. Fig. 4(c) presents the temperature distribution when the waveguide reaches equilibrium at 100 ms. The effective RI modulation of the TE$_0$ mode for the probe laser at 1550 nm is estimated to be 2.7×10^{-8}, corresponding to 10 mrad phase modulation for the 91.2 mm waveguide.

2.4. Heterodyne interferometry

The wavelength modulation of the pump laser generates periodic heating of the waveguide and subsequently leads to the phase modulation of the probe laser propagating in the same waveguide. For on-chip PTS, the phase modulation $\Delta\varphi$ is determined by:

$$\Delta\varphi \propto I_{pump} \Gamma_{air} \alpha(v) \tag{2}$$

where I_{pump} is the pump laser intensity, and $\alpha(v)$ is the gas absorbance. The phase modulation can be sensitively detected by a heterodyne interferometer. The probe beam E_1 and a localized oscillator E_2 are expressed as:

$$E_1 = A_1 \bullet \cos(w_1 \bullet t + \Delta\varphi) \tag{3}$$

$$E_2 = A_2 \bullet \cos(w_2 \bullet t) \tag{4}$$

where A_1, A_2 are the amplitude, w_1, w_2 is the frequency. The interferometric signal of E_1 and E_2 on a photodetector could be expressed:

$$i = G\left\{ \frac{A_1^2}{2} + \frac{A_2^2}{2} + A_1 \bullet A_2 \bullet \cos(\Omega \bullet t + \Delta\varphi) \right\} \tag{5}$$

where $\Omega = w_1 - w_2$ is the beat note frequency within the RF range. G is the gain of the photodetector. Eq. (5) reveals that the phase variation $\Delta\varphi$ still remains in the beat note, which could be easily extracted with a lock-in amplifier. The extracted phase variation consists of the wavelength modulated gas absorbance signal could be further obtained by detecting the 2nd harmonics (PTS-2f). More details on harmonic
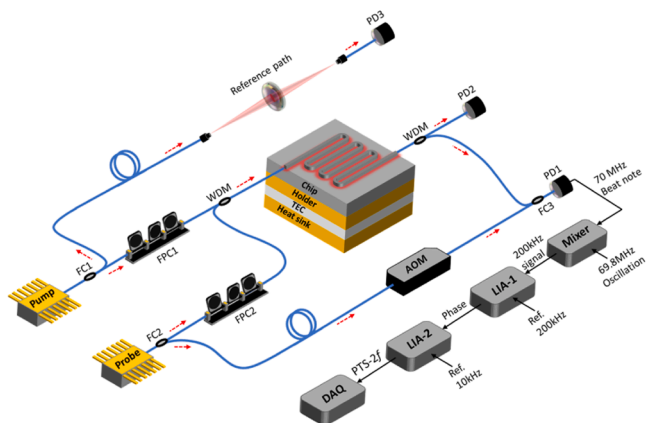

Fig. 2. Cavity mode around 2004 nm of the LN ring resonator.
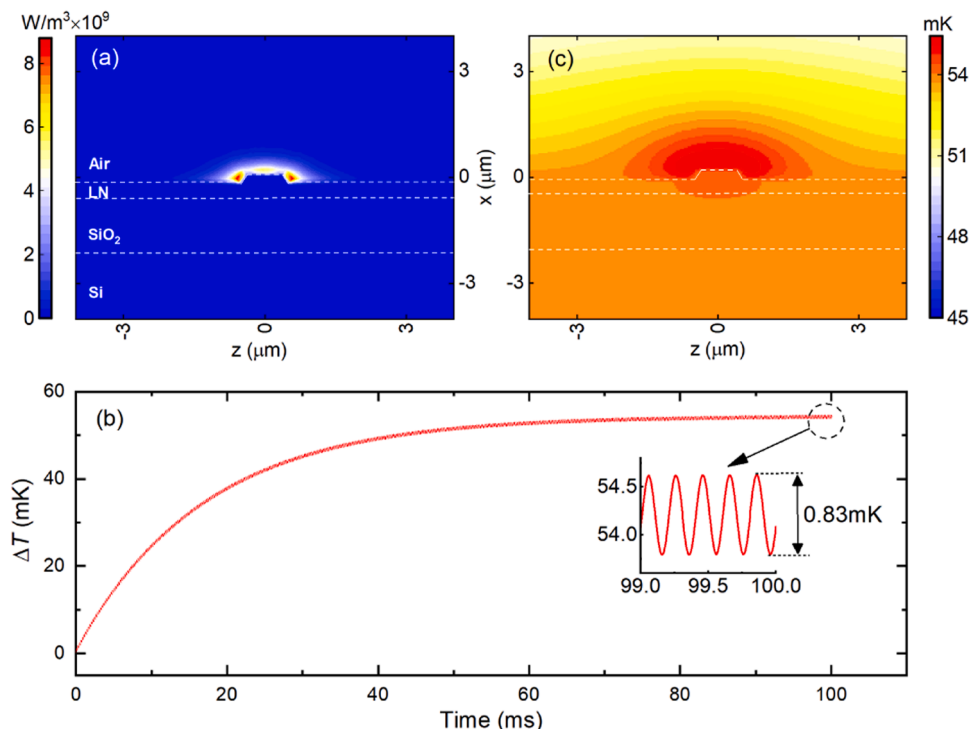
Fig. 4. (a) Simulated heat source distribution in the LN waveguide caused by CO_2 absorption of a 1-mW pump laser at 2004 nm. The heat source is sinusoidally modulated as $Q' = Q(1+sin(2\pi ft))/2$, where f is the modulation frequency of the pump laser. (b) Time-dependent temperature variation of the LN waveguide. Inset: the magnified region between 99-100 ms. (c) Temperature distribution at 100 ms of the heat transfer process.

detection of the photothermal heterodyne signals can be found in the literature [33].

3. Experimental setup

Fig. 5 depicts the schematic of the on-chip photothermal heterodyne gas sensing experiment. A distributed feedback diode laser (NEL) is sinusoidally modulated at 5 kHz and its wavelength is slowly triangle-scanned at 250 mHz to cover the R(16) absorption line of CO_2 at 2004 nm. A probe laser at 1550 nm (RIO Lasers) where there is no CO_2 gas absorption, is used in the heterodyne interferometer. The pump and probe beams are coupled with a wavelength division multiplexer (WDM) and further coupled into and out of the LN waveguide via two lensed fibers. The lensed fibers are mounted on two XYZ-motorized stages for

the coupling alignment. Two fiber polarization controllers (FPCs) are used for the pump and probe beams to achieve the TE_0 mode propagation in the LN waveguide. The LN rib waveguide is placed in the sensing arm, whereas the reference arm is frequency-shifted by 70 MHz using an acousto-optic modulator (AOM, model F-YSG70–2, CETC). The heterodyne output (PD1, PDA05CF2, Thorlabs) generates a beat note signal at 70 MHz. The demodulation is implemented by using two cascaded lock-in amplifiers (LIA-1 and LIA-2). The 70 MHz beat note is first down-shifted to 200 kHz by mixing with a 69.8 MHz local oscillator, which is further demodulated by the lock-in amplifier (LIA-1) to obtain the phase variation $\Delta\varphi$. Finally, another lock-in amplifier (LIA-2) is used to demodulate the second harmonic photothermal signal (PTS-2f) at 10 kHz. The cut-off frequencies of low-pass filters inside the two LIAs are set to be 50 kHz and 1.25 Hz, respectively.

The LN chip is fixed on a brass holder with the temperature actively controlled (stability ± 10 mK) by a thermoelectric cooler (TEC). The LN chip and two stages for coupling alignment are enclosed in a sealed chamber that can be filled with the target gas mixtures (more details are provided in Supplementary Note 3). A free-space path of 120 mm is used as a reference measurement inside the same chamber. It should be noted that the gas changeover time exceeded 10 min in this demonstration due to the large chamber volume and gas mixing process. A short response time can be achieved by packaging the chip in a compact gas cell in the future.

4. Results and discussion

We show the drastically improved SNR of gas on-chip detection using the proposed PTS approach compared to the traditional absorption spectroscopy. The transmitted signal (PD2, PDA10D2, Thorlabs) of edge-coupled integrated photonic waveguides commonly sees substantial interference fringes due to light reflections between the two wave-guide facets. As shown in Fig. 6, with pure nitrogen filled in the gas chamber, the fringe pattern varies significantly even at a small temperature change of 2°C, demonstrating a spectral shift of 0.09 cm^{-1}/K.

Fig. 5. Experimental setup of on-chip photothermal spectroscopy with het-erodyne detection. FC: fiber coupler (splitting ratio 90/10); WDM: wavelength division multiplexing; AOM: acousto-optic modulator; PD: photodetector. LIA: lock-in amplifier.
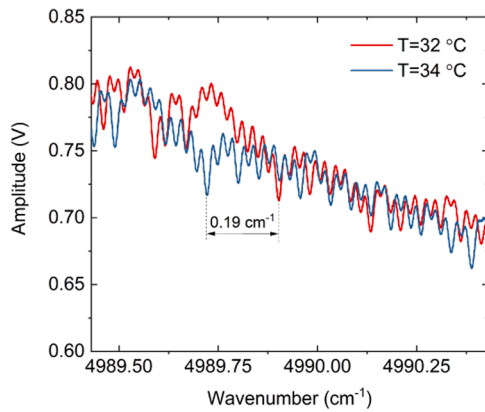
Fig. 6. Measured transmission signal (pure N_2) of the pump light through the LN waveguide at 32 °C and 34 °C, respectively.

By modulating the pump laser at 5 kHz, Fig. 7(a) shows the demodulated 2nd-harmonic signals of wavelength modulation spectroscopy (WMS-2*f*) of 54% CO_2 at two different chip temperatures. The WMS-2*f* signals are significantly distorted since absorption measurement is directly determined by the laser intensity that is much more sensitive to the interference fringe noise. In contrast, the heterodyne photothermal 2nd-harmonic (PTS-2*f*) measurement shows much improved SNR under the same experimental condition, as shown in Fig. 7(b). The non-zero background under N_2 environment is observed due to the inherent nonlinearities, such as Kerr effect, photorefractive effect and thermo-optic effect of the waveguide material. It is important to note that these nonlinearities exhibit a flat behavior within the target gas spectrum range, acting as a flat DC component that can be effectively filtered by the low-pass filter integrated within the lock-in amplifier. Conversely, the gas absorption spectrum displays a distinct line-shape with a notably narrow linewidth, allowing for easy extraction. In practical terms, these nonlinearities are power dependent, and the interference fringe can induce intensity variations within the gas spectrum range, potentially introducing residual 2nd harmonics in the photothermal detection. Fortunately, these nonlinearities induced background is stable and can be subtracted as background from the measurement.

Fig. 8 presents a comprehensive comparison of the long-term noise measurements under N_2 environment for both absorption and photothermal detection. The findings obtained from absorption detection

demonstrate significant random signal drift with a large amplitude, as depicted in Fig. 8(a). The corresponding Allan deviation analysis, depicted in Fig. 8(c), also indicates the rapid divergence in stability over time. In contrast, for photothermal detection, as illustrated in Fig. 8(b), the noise behaves like white noise since only the photothermal-induced phase modulation signal can be picked up by the heterodyne interferometer, effectively mitigating the interference fringe. The Allan deviation analysis also proves that the photothermal detection exhibit substantial long-term stability and achieve a detection limit of 870 ppm with 190 s averaging time, as shown in Fig. 8(d). While the absorption spectroscopy appears to show a detection limit of 4460 ppm with a short averaging time, the observed significant drift in absorption detection renders its sensitivity unreliable for practical applications.

The photothermal measurements are then repeated at different CO_2 concentration shown in Fig. 9(a). The results indicate the linear response of the PTS-2*f* amplitude to CO_2 concentration between 6.8% and 54%. Based on the input pump power (8 mW), 1σ noise level (1.33μV), and detection bandwidth (1.44 Hz), we estimate a normalized noise equivalent absorption coefficient (NNEA) of 9.3×10^{-6} cm^{-1}•W•Hz$^{-1/2}$. It should be noted that absorption saturation may lead to decreased absorption at high incident intensity, which could potentially occur in the on-chip detection due to the confinement of laser power within the nano-waveguide. To explore the saturation effect, we conducted observations of photothermal responses under varying input pump laser powers, as depicted in Fig. 9(b). Notably, the photothermal signals exhibited a highly linear response without any significant offset, suggesting the absence of any saturation effect in our study.

It is of interest to discuss the possible aspects of obtaining a higher SNR so that the on-chip PTS becomes more feasible for trace gas sensing. Firstly, optimize the waveguide length according to the propagation loss. The photothermal induced RI change $\Delta n \propto P_{pump}(L)$, where P_{pump} is the pump laser power inside the waveguide which is related to the propagation loss and waveguide length L. So, the accumulated phase change can be expressed as:

$$\varphi \propto \int_0^L P_{pump}(L) \bullet \frac{2\pi}{\lambda} \bullet n_{eff} \bullet L \quad dL \qquad (6)$$

For the propagation loss of 1.2 dB/cm, the relationship between phase change and waveguide length is shown in Fig. 10(a). The analysis shows that the phase accumulation tends to plateau as the waveguide length exceeds 30 cm. In our experiment, the waveguide length is fabricated as 9.12 cm for a proof concept. Moreover, Fig. 10(b) depicts the relationship between phase accumulation and propagation loss,
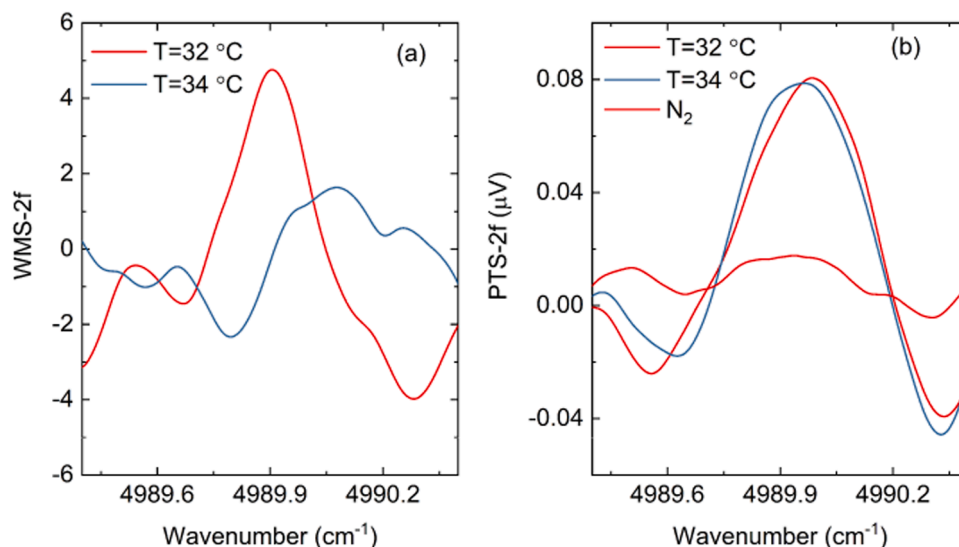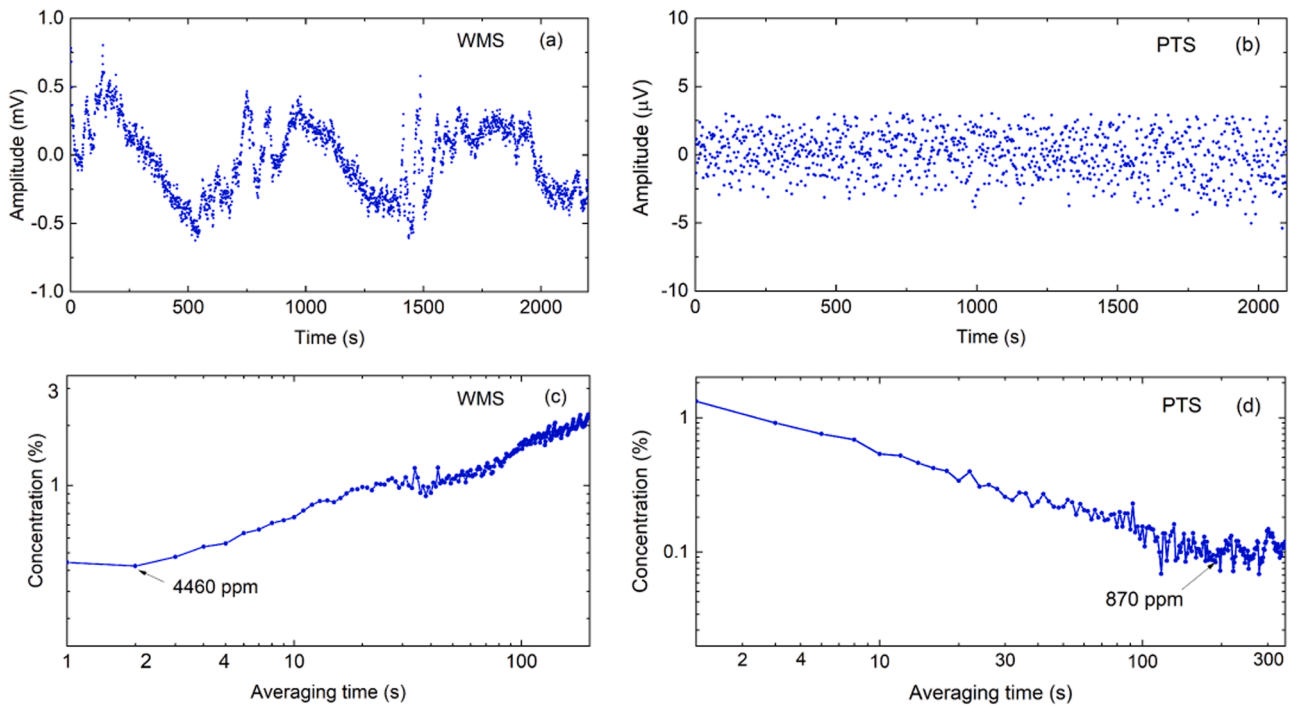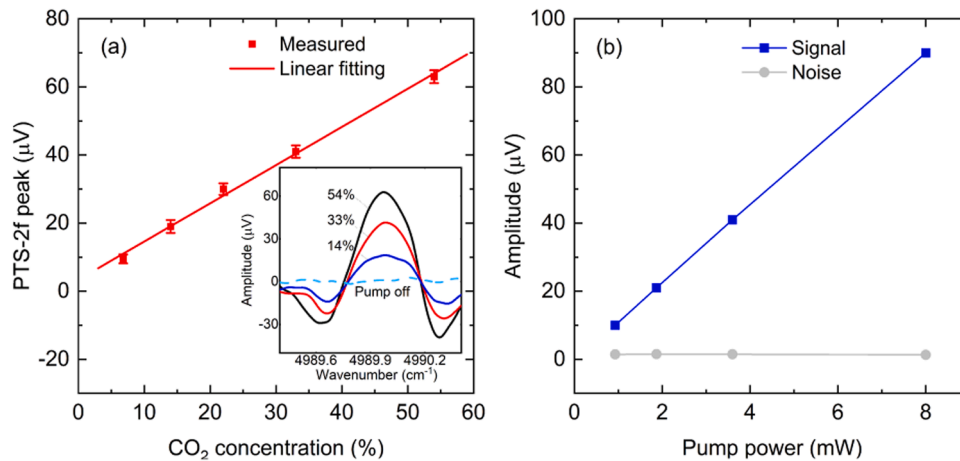

Fig. 7. (a) Absorption signal (WMS-2*f*) of 54% CO_2. (b) Photothermal signal (PTS-2*f*) of 54% CO_2.

Fig. 8. (a) long-term noise with absorption detection. (b) long-term noise with photothermal detection (c) Allan deviation of absorption detection (d) Allan deviation of photothermal detection. Measurements are conducted under N_2 environment.

Fig. 9. (a) Variation of the PTS-$2f$ peak amplitude with CO_2 concentration. Inset: representative PTS-$2f$ spectra measured under different CO_2 concentrations. (b) Variation of the PTS-$2f$ peak-to-peak amplitude with the pump power level with a fixed 54% CO_2. The noise remains almost unchanged at different power levels.

indicating that the sensing performance can be largely improved by reducing the propagation loss. This can be achieved to refine the side-wall roughness by optimized dry etching fabrication process [34], post-etch cleaning [35] and chemical mechanical polishing [36]. And a high-power pump laser could be implemented for higher sensitivity as the PTS signal increases linearly with the pump power while the noise remains almost unchanged at different power levels, as shown in Fig. 9 (b). And LN waveguide is capable to handle 10 W-level optical power without optical damage [37]. The coupling loss can also be reduced by using a high-NA free-space focusing lens or adiabatic mode spot-size converter [38].

Secondly, a higher evanescent field factor in the air-cladding could be designed to enhance the light-matter interaction. The current waveguide features a measured evanescent field factor of 6.9% in the air-cladding (Supplementary Note 4), which could be increased to 16% by designing a suspended waveguide structure (Supplementary Note 2). It

also helps maintain the absorption-induced heat production within the suspended structure to improve the sensitivity (Supplementary Note 2). Note that a larger evanescent field may introduce a larger propagation loss, which should be evaluated systematically in the sensor design.

Thirdly, with a suspended waveguide structure, the sensitivity can be largely enhanced by migrating the sensing wavelength to mid-infrared of 4.3 μm where the line strength of CO_2 shows three orders of magnitude larger than that at 2 μm. Additionally, the environmental disturbance would introduce polarization noise in the fiber-optic interferometry. This problem could be mitigated by using polarization maintenance fibers or implementing on-chip interferometry.

5. Conclusion

In summary, we report for the first time on-chip photothermal spectroscopy for sensitive gas detection on a nanophotonic LN platform.
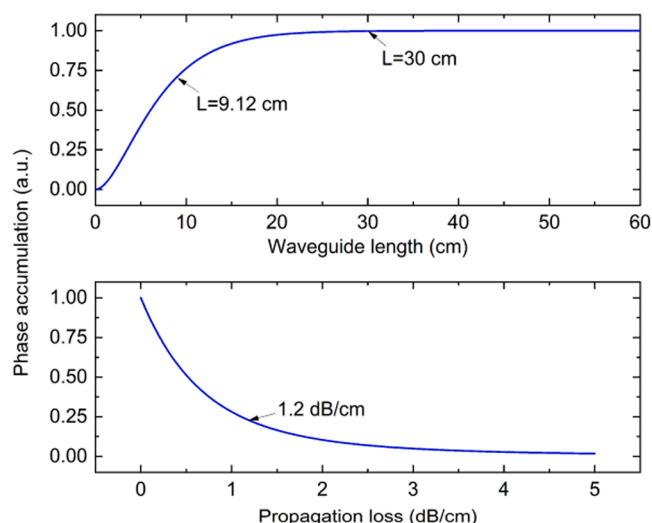
Fig. 10. Phase accumulation versus (a) varied waveguide length, propagation loss is set to be 1.2 dB/ cm. (b) varied propagation loss, waveguide length is set to be 9.12 cm. The vertical coordinates are normalized for comparison purpose.

Compared to on-chip absorption spectroscopy, our method shows dramatically improved SNR due to the significantly reduced fringe noise. With a 91.2 mm long LN rib waveguide, we achieve a detection limit of 870 ppm CO_2 at 190 s integration time, and demonstrate the sensor robustness under the disturbance of chip temperature. Different from on-chip absorption spectroscopy which is limited by the absorption path length, on-chip PTS could potentially overcome this limitation by using more sensitive phase detection methods. For instance, a micro-resonator-based interferometer can be monolithically integrated in a single chip for higher sensitivity [39]. More importantly, LN integrated photonics platform could support on-chip interferometer locking due to its high and fast electro-optical response [40]. Finally, we expect to further extend this method to advanced light sources such as Kerr combs to generate highly sensitive broadband on-chip gas sensing systems. Hence, our study opens an opportunity to realize compact, sensitive, robust and smart on-chip gas detection for many applications such as smart homes, point-of-care disease diagnostics and wearable devices.

CRediT authorship contribution statement

Yan Yue: Writing – review & editing, Writing – original draft, Validation, Methodology, Conceptualization. **Ren Wei:** Writing – review & editing, Supervision, Project administration, Methodology, Funding acquisition, Conceptualization. **Feng Hanke:** Writing – original draft, Resources, Methodology, Conceptualization. **Wang Cheng:** Writing – review & editing, Supervision, Resources, Project administration, Funding acquisition, Conceptualization.

Declaration of Competing Interest

The authors declare that they have no known competing financial interests or personal relationships that could have appeared to influence the work reported in this paper.

Data availability

Data will be made available on request.

Acknowledgements

Appendix A. Supporting information

Supplementary data associated with this article can be found in the online version at doi:10.1016/j.snb.2024.135392.

References

[1] J.W. Wu, G.C. Yue, W.C. Chen, Z.K. Xing, J.Q. Wang, W.R. Wong, et al., On-chip optical gas sensors based on group-IV materials, ACS Photonics 7 (2020) 2923–2940.

[2] C. Zheng, M. Pi, F. Song, Y. Li, Z. Peng, G. Guan, et al., Recent progress in infrared absorption spectroscopy for gas sensing with discrete optics, hollow-core fibers and on-chip waveguides, J. Light. Technol. (2023).

[3] J.-W. Yoon, J.-H. Lee, Toward breath analysis on a chip for disease diagnosis using semiconductor-based chemiresistors: recent progress and future perspectives, Lab Chip 17 (2017) 3537–3557.

[4] A. Hänsel, M.J. Heck, Opportunities for photonic integrated circuits in optical gas sensors, J. Phys. Photonics 2 (2020) 012002.

[5] J. Lin, F. Bo, Y. Cheng, J. Xu, Advances in on-chip photonic devices based on lithium niobate on insulator, Photonics Res. 8 (2020) 1910–1936.

[6] D.S. Su, D.P. Tsai, T.J. Yen, T. Tanaka, Ultrasensitive and selective gas sensor based on a channel plasmonic structure with an enormous hot spot region, ACS Sens 4 (2019) 2900–2907.

[7] M. Vlk, A. Datta, S. Alberti, H.D. Yallew, V. Mittal, G.S. Murugan, et al., Extraordinary evanescent field confinement waveguide sensor for mid-infrared trace gas spectroscopy, Light Sci. Appl. 10 (2021) 26.

[8] M. Pi, C. Zheng, H. Zhao, Z. Peng, G. Guan, J. Ji, et al., Ultra-wideband mid-infrared chalcogenide suspended nanorib waveguide gas sensors with exceptionally high external confinement factor beyond free-space, ACS Nano 17 (2023) 17761–17770.

[9] L. Tombez, E.J. Zhang, J.S. Orcutt, S. Kamlapurkar, W.M.J. Green, Methane absorption spectroscopy on a silicon photonic chip, Optica 4 (2017) 1322–1325.

[10] E.J. Zhang, Y. Martin, J.S. Orcutt, C. Xiong, M. Glodde, N. Marchack, et al., Monolithically integrated silicon photonic chip sensor for near-infrared trace-gas spectroscopy, Proc. SPIE 11010 (2019) 110100B.

[11] B. Hinkov, F. Pilat, L. Lux, P.L. Souza, M. David, A. Schwaighofer, et al., A mid-infrared lab-on-a-chip for dynamic reaction monitoring, Nat. Commun. 13 (2022) 4753.

[12] C.C. Teng, E.J. Zhang, C. Xiong, W.M.J. Green, G. Wysocki, Dynamic computational optical fringe mitigation in tunable laser absorption spectroscopy, Opt. Express 28 (2020) 39017–39023.

[13] E.J. Zhang, L. Tombez, C.C. Teng, G. Wysocki, W. Green, Adaptive etalon suppression technique for long-term stability improvement in high index contrast waveguide-based laser absorption spectrometers, Electron. Lett. 55 (2019) 851–853.

[14] C.C. Teng, C. Xiong, E.J. Zhang, W.M. Green, G. Wysocki, Adaptive thermal stabilization of an integrated photonic spectrometer using parasitic interference fringes, Opt. Lett. 45 (2020) 3252–3255.

[15] S.E. Bialkowski, N.G. Astrath, M.A. Proskurnin, Photothermal spectroscopy methods, John Wiley & Sons, 2019.

[16] Y. Qi, F. Yang, Y. Lin, W. Jin, H.L. Ho, Nanowaveguide enhanced photothermal interferometry spectroscopy, J. Light. Technol. 35 (2017) 5267–5275.

[17] J.P. Waclawek, C. Kristament, H. Moser, B. Lendl, Balanced-detection interferometric cavity-assisted photothermal spectroscopy, Opt. Express 27 (2019) 12183–12195.

[18] W. Jin, Y. Cao, F. Yang, H.L. Ho, Ultra-sensitive all-fibre photothermal spectroscopy with large dynamic range, Nat. Commun. 6 (2015) 6767.

[19] M. Hu, A. Ventura, J.G. Hayashi, F. Poletti, S. Yao, W. Ren, Trace gas detection in a hollow-core antiresonant fiber with heterodyne phase-sensitive dispersion spectroscopy, Sens. Actuators B Chem. 363 (2022) 131774.

[20] Q. Wang, Z. Wang, H. Zhang, S. Jiang, Y. Wang, W. Jin, et al., Dual-comb photothermal spectroscopy, Nat. Commun. 13 (2022) 2181.

[21] D. Zhu, L. Shao, M. Yu, R. Cheng, B. Desiatov, C. Xin, et al., Integrated photonics on thin-film lithium niobate, Adv. Opt. Photonics 13 (2021) 242–352.

[22] A. Boes, L. Chang, C. Langrock, M. Yu, M. Zhang, Q. Lin, et al., Lithium niobate photonics: Unlocking the electromagnetic spectrum, Science 379 (2023) eabj4396.

[23] M. Seiter, D. Keller, M.W. Sigrist, Broadly tunable difference-frequency spectrometer for trace gas detection with noncollinear critical phase-matching in LiNbO3, Appl. Phys. B 67 (1998) 351–356.

[24] J.Y. Zhang, Y.M. Sua, J.Y. Chen, J. Ramanathan, C. Tang, Z. Li, et al., Carbon-dioxide absorption spectroscopy with solar photon counting and integrated lithium niobate micro-ring resonator, Appl. Phys. Lett. 118 (2021) 171103.

[25] D. Pohl, M.R. Escale, M. Madi, F. Kaufmann, P. Brotzer, A. Sergeyev, et al., An integrated broadband spectrometer on thin-film lithium niobate, Nat. Photonics 14 (2020) 24–29.

[26] C. Wang, M. Zhang, M.J. Yu, R.R. Zhu, H. Hu, M. Loncar, Monolithic lithium niobate photonic circuits for Kerr frequency comb generation and modulation, Nat. Commun. 10 (2019) 978.

[27] M. Zhang, B. Buscaino, C. Wang, A. Shams-Ansari, C. Reimer, R.R. Zhu, et al., Broadband electro-optic frequency comb generation in a lithium niobate microring resonator, Nature 568 (2019) 373–377.

[28] D.E. Zelmon, D.L. Small, D. Jundt, Infrared corrected Sellmeier coefficients for congruently grown lithium niobate and 5 mol.% magnesium oxide–doped lithium niobate, JOSA B 14 (1997) 3319–3322.

[29] J. Kischkat, S. Peters, B. Gruska, M. Semtsiv, M. Chashnikova, M. Klinkmüller, et al., Mid-infrared optical properties of thin films of aluminum oxide, titanium dioxide, silicon dioxide, aluminum nitride, and silicon nitride, Appl. Opt. 51 (2012) 6789–6798.

[30] J.T. Robinson, K. Preston, O. Painter, M. Lipson, First-principle derivation of gain in high-index-contrast waveguides, Opt. Express 16 (2008) 16659–16669.

[31] P.E. Ciddor, Refractive index of air: new equations for the visible and near infrared, Appl. Opt. 35 (1996) 1566–1573.

[32] L. Moretti, M. Lodice, F.G.D. Corte, I. Rendina, Temperature dependence of the thermo-optic coefficient of lithium niobate, from 300 to 515 K in the visible and infrared regions, J. Appl. Phys. 98 (2005) 253–276.

[33] C. Yao, S. Gao, Y. Wang, W. Jin, W. Ren, Heterodyne interferometric photothermal spectroscopy for gas detection in a hollow-core fiber, Sens. Actuators B Chem. 346 (2021) 130528.

[34] S.Y. Siew, E.J.H. Cheung, H. Liang, A. Bettiol, N. Toyoda, B. Alshehri, et al., Ultra-low loss ridge waveguides on lithium niobate via argon ion milling and gas clustered ion beam smoothening, Opt. Express 26 (2018) 4421–4430.

[35] M. Zhang, C. Wang, R. Cheng, A. Shams-Ansari, M. Lončar, Monolithic ultra-high-Q lithium niobate microring resonator, Optica 4 (2017) 1536–1537.

[36] R. Wolf, I. Breunig, H. Zappe, K. Buse, Scattering-loss reduction of ridge waveguides by sidewall polishing, Opt. Express 26 (2018) 19815–19820.

[37] M. Zhang, C. Wang, P. Kharel, D. Zhu, M. Lončar, Integrated lithium niobate electro-optic modulators: when performance meets scalability, Optica 8 (2021) 652–667.

[38] Y. Fu, T. Ye, W. Tang, T. Chu, Efficient adiabatic silicon-on-insulator waveguide taper, Photonics Res. 2 (2014) A41–A44.

[39] A. Vasiliev, A. Malik, M. Muneeb, B. Kuyken, R. Baets, Gn Roelkens, On-chip mid-infrared photothermal spectroscopy using suspended silicon-on-insulator microring resonators, ACS Sens 1 (2016) 1301–1307.

[40] G. Martin, S. Heidmann, J.-Y. Rauch, L. Jocou, N. Courjal, Electro-optic fringe locking and photometric tuning using a two-stage Mach–Zehnder lithium niobate waveguide for high-contrast mid-infrared interferometry, Opt. Eng. 53 (2014) 034101.

Yue Yan received his B.S. and M.S. degree from NanChang University and Tianjin University. He is currently working toward the Ph.D. degree with the Department of Mechanical and Automation Engineering, The Chinese University of Hong Kong, Hong Kong. His research interests include optical sensing and laser spectroscopy.

Hanke Feng received his B.S. and M.S. degree from Xi'an University of Technology and Xi'an Jiaotong University. He is currently working toward the Ph.D. degree with the Department of Electrical Engineering, City University of Hong Kong, Hong Kong. His research interest focuses on design and nanofabrication technology of integrated lithium niobate photonic circuits.

Cheng Wang received his B.S. degree in Microelectronics from Tsinghua University, Beijing, China, in 2012 and the Ph.D. degree in Electrical Engineering from Harvard University, in 2017. From 2017 – 2018, Cheng conducted research as a postdoctoral fellow at Harvard, before joining City University of Hong Kong as an Assistant Professor in June 2018. Dr. Wang's research focuses on the design and nanofabrication technology of integrated photonic devices and circuits. His current research effort focuses on realizing integrated lithium niobate photonic circuits for applications in optical communications, millimeter-wave/terahertz technologies, nonlinear optics, and quantum photonics.

Wei Ren received the B.S. degree in mechanical engineering and automation from Tsinghua University, Beijing, China, in 2006, and the Ph.D. degree in mechanical engineering from Stanford University, Stanford, CA, USA, in 2013. He is currently an Associate Professor with the Department of Mechanical and Automation Engineering, The Chinese University of Hong Kong, Hong Kong. After the graduation degree, he was a Postdoctoral Fellow with the Department of Electrical and Computer Engineering, Rice University, Houston, TX, USA. His research interests include laser spectroscopy, optical sensing, and combustion and propulsion. He is a Senior Member of Optica.